Flow boiling characteristics in plain and porous coated microchannel heat sinks

Vivian Y.S. Lee[a], Gary Henderson[b], Alex Reip[c], Tassos G. Karayiannis[a,*]

[a] Brunel University London, Kingston Lane, Uxbridge, Middlesex UB8 3PH, UK
[b] TMD Technologies Ltd., Swallowfield Way, Hayes, Middlesex, UB3 1DQ, UK
[c] Oxford nanoSystems Ltd., Blacklands Way, Abingdon, Oxfordshire, OX14 1DY, UK

ARTICLE INFO

ABSTRACT

Flow boiling heat transfer enhancement using porous coatings in microchannels has been experimentally investigated with HFE-7200. Results of the coated microchannel heat sink were compared to baseline results in a plain, micro-milled copper microchannel heat sink at similar operating conditions, namely inlet pressure of 1 bar, mass flux of 200 – 400 kg/m^2 s and inlet subcooling of 10 K at wall heat fluxes between 24.5 kW/m^2 to 206.6 kW/m^2. Flow visualisation results and SEM surface analysis are presented. The coated surface was densely populated with well-defined cavities between 0.6 μm to 3.3 μm wide. The plain channels had fewer cavities for a given area and these were larger, i.e. up to 6 μm. Bubble generation frequency in the coated channels is significantly higher than in the plain channels due to the presence of more favourable nucleation sites on the coated surface. Flow pattern development occurred similarly in both heat sinks, namely bubbly to slug, churn and annular flow with increasing heat flux, with earlier flow pattern transitions in the coated heat sink. Enhancement in microchannel flow boiling heat transfer was shown to be influenced by mass velocity and may reach up to 44% at low heat fluxes, where the nucleate boiling mechanism is dominant. It diminishes with increasing heat flux, corresponding to nucleate boiling suppression following flow regime transition. Pressure drop increase posed by the coated heat sink is relatively small in terms of overall system power consumption but appears to be influenced by mass flux, pressure oscillations as well as channel rewetting behaviour.

© 2021 The Author(s). Published by Elsevier Ltd.
This is an open access article under the CC BY license (http://creativecommons.org/licenses/by/4.0/)

1. Introduction

Efficient thermal management of high-power density devices constitutes a bottleneck in electronics miniaturization, where heat fluxes could reach several MW/m^2, Karayiannis and Mahmoud [1]. Traditional cooling strategies are insufficient in dissipating concentrated heat loads on modern high-power chips. This tends to limit the peak power output of a device in fear of compromising the junction temperature limit, reliability and performance of the device. Flow boiling in high surface-area to volume ratio microchannel heat sinks is a promising technique to manage high heat fluxes encountered in modern electronic devices and has been extensively studied, as reviewed in [1]. Nonetheless, issues such as flow instability, high boiling incipience temperature, dryout and critical heat flux as well as general predictive correlations for heat transfer and pressure drop need to be considered for this technique for compact cooling of miniaturised power components.

Some of these issues relate to bubble nucleation dynamics and surface wettability in the channel, and as explained in pool boiling work, surface defects and imperfections are favourable sites for bubble nucleation due to vapour entrapment [2]. Therefore, surface modification techniques such as altering surface roughness using sandpaper treatment, fabrication of artificial cavities and surface coatings have been employed to produce surface topologies with nucleation sites that may help to lower boiling incipient superheat, augment heat transfer and improve the critical heat flux limit, as concluded in Khan et al. [3], Shojaeian and Kosar [4] and more recently in Liang and Mudawar [5]. These were achieved mainly through (i) an increase in nucleation site density and (ii) altered surface wettability on modified surfaces compared to smooth surfaces, where enhanced capillary wicking delayed critical heat flux, especially in cases where annular flow dominates. Notably for the latter, the effect of modifications in surface wettability, including biphillic surfaces [6], in order to influence boiling behaviour, is typically insignificant in cases where highly wetting refrigerants and fluids (contact angle < 10°) are employed, as compared to water (where contact angle may approach 120°). Importantly, an efficient

---

* Corresponding author.
  E-mail address: tassos.karayiannis@brunel.ac.uk (T.G. Karayiannis).

Nomenclature

D_h	hydraulic diameter [m]
ΔP	pressure drop [kPa]
$E_{ht\%}$	heat transfer enhancement percentage [%]
G	mass flux [kg/m^{2}s]
H_{ch}	channel height [m]
$h_{(z)}$	local heat transfer coefficient [W/m^2 K]
$\bar{h}_{tp}$	average heat transfer coefficient [W/m^2 K]
L	length [m]
N	number of channels [-]
q''	heat flux [W/m^2]
$T_{f(z)}$	local fluid temperature [°C]
$T_{w(z)}$	temperature of channel bottom wall [°C]
W	width [m]
x	vapour quality [-]
z/L	dimensionless axial location [-]
η	fin efficiency [-]
ρ_g	gas density [kg/m^3]

Subscripts

b	base
ch	channel
coated	coated microchannel
f	fin
hs	heat sink
loss	pressure losses in manifold
meas	measured pressure drop
pen	penalty
plain	plain microchannel
sat	saturated
sp	single-phase
sub	subcooled
tp	two-phase
w	wall

heat transfer coating must be cost effective and should only result in a reasonable pressure drop penalty in proportion to the yield in heat transfer enhancement, in view of the power consumption of the cooling system. Heat transfer coatings must also demonstrate durability over a wide range of operating conditions [3,5]. In particular, the deformation of carbon nanotubes [7,8] and gradual detachment of nanoparticle coatings [9,10] have been reported at high mass fluxes as well as following the occurrence of critical heat flux. Whilst the use of inlet restrictors has also been demonstrated to mitigate flow boiling instabilities and improve critical heat flux limit, it comes at a significant cost of pressure drop [11] and even decreased heat transfer performance in microchannel heat sinks [12]. On the other hand, surface coatings are easier to apply on conventionally-machined microchannel heat sinks and provide similar benefits to inlet restrictors, i.e. increased nucleation site density and promotion of stable flow regimes that may enhance heat transfer performance as well as delay the occurrence of critical heat flux. For example, Bai et al. [13] found that their sintered porous coating suppressed flow instability in microchannels due to smaller bubble departure diameters from the coated surface, which reduced coalescence and the formation of large bubbles that induces flow reversal in microchannels."

Hsu [13] as early as 1962 proposed a model to predict the size range of active nucleation sites on a heated surface. The model predicts that for a given working fluid and wall superheat condition, only a limited size range of nucleation sites may be activated to initiate bubble nucleation, i.e. boiling incipience on a heated surface. Surface characteristics may be optimised (to a certain degree bearing in mind that this was developed for pool boiling) using

this model, to provide an even distribution of cavities within the appropriate size range on the heated substrate. Surface coatings represent a more controlled method of cavity population compared to surface roughness modification using the sandpaper technique and less complex compared to fabricating artificial nucleation sites in narrow passages [14,15]. Porous coatings have been shown to improve flow boiling heat transfer coefficients by up to 178% using water [16]. The enhancement in two-phase heat transfer characteristics are typically attributed to the presence of preferable nucleation conditions for bubble formation, beneficial especially in the nucleate boiling regime. Furthermore, boiling incipience wall superheat may be lowered by between 6 K to 8 K, as reported in [16]–[18] for various working fluids, which could help suppress two-phase flow instabilities related to explosive boiling in multi-microchannel heat sinks [19]. The critical heat flux limit is typically enhanced by improving surface wettability using coatings. However, as mentioned above, the effect of coatings on wettability characteristics is limited where naturally wetting fluids, i.e. most refrigerants, are employed. For instance, Yang et al. [20] obtained up to 300% increase in critical heat flux using a silicon nanowire coating with water, but only up to 16% enhancement with HFE-7000 using the same coating [21].

Heat transfer enhancement by means of porous coatings is generally found to be more effective in the nucleate boiling regime, i.e. at low vapour qualities, as reported using porous copper coatings in [17,18]. Sun et al. [17] observed an increase in flow boiling heat transfer coefficients at the outlet of the channel by up to 692% using a sintered copper coating layer with a mean particle diameter of 50 μm on the bottom surface of a 0.9 mm hydraulic diameter channel and fluid FC-72. The highest augmentation was obtained at low vapour qualities just after the onset of boiling, i.e. x ∼ 0.1, and depreciated steeply with increasing vapour quality. The decrease in heat transfer coefficients with vapour quality in the coated section was attributed to bubble confinement, which suppressed nucleate boiling and induced local dryout in the channel. Bai et al. [18] observed an increase of around 81% in the local flow boiling heat transfer coefficients of ethanol with a sintered copper coating with a characteristic particle diameter of 55 μm on the bottom surfaces of a parallel channel array (0.54 mm hydraulic diameter), in relation to bare copper channels at very low vapour qualities of around 0.02. In contrast to the plain copper channels, where heat transfer coefficients remained relatively constant with vapour quality, heat transfer coefficients in the coated channels decreased significantly with increasing vapour quality, and resulted in a reduced enhancement effect. Whilst no flow pattern results were presented, the authors argued that this was due to the change in heat transfer mechanism corresponding to flow regime development in the channels. Experiments were only conducted for low vapour qualities up to 0.3. Surface modification on the channel side walls was studied by Bortolin et al. [24] for R134a, reporting lower temperature overshoot and a 40% increase in the heat transfer coefficient.

From the results above, it is evident that the enhancement effect appears to be influenced by operating conditions such as heat flux and mass flux, owing to their respective effects on flow pattern development in microchannels. Varying heat transfer enhancement results at different heat fluxes and mass velocities were also reported in [22,23] for silicon nanowires. Wang et al. [22] etched silicon nanowires on the side and bottom walls of a parallel silicon channel array with nominal widths and depths of 0.25 mm. The degree of wall superheat at a given heat flux and mass flux condition was reduced by around 15 K from 75 K to just over 60 K in the silicon nanowire-coated channels. The flow boiling heat transfer enhancement of water was relatively unchanged with heat flux at a mass flux of 250 kg/m^{2}s and increased slightly at high heat fluxes. This is due to the prevention of wall dryout

with capillary-assisted rewetting provided by the nanowires. At a higher mass flux of 500 kg/m^{2}s, a peak enhancement effect of around 134% is recorded at a base heat flux of around 1000 kW/m^2 but decreases notably to just over 105% on approaching the critical heat flux limit. The smaller enhancement effect at the higher mass flux condition was suspected to be due to contamination-related degradation of surface wettability of the coated surface during experiments. Similarly, Li et al. [23] used silicon nanowires to improve the surface wettability on the bottom surface of their silicon microchannel array, consisting of 14 channels with nominal width and height of 0.25 mm and 0.2 mm respectively. The silicon nanowires were found to agglomerate and formed cavities in the order of several micrometres wide, which served as favourable boiling nucleation sites. The flow boiling characteristics of water at mass fluxes ranging from 119 kg/m^{2}s to 571 kg/m^{2}s were investigated in a plain silicon and nanowire-coated channel array. Heat transfer coefficients in the coated channels after boiling incipience were actually lower compared to the plain channel array at a mass flux of 119 kg/m^{2}s. Nonetheless, at mass fluxes between 238 kg/m^{2}s and 571 kg/m^{2}s, heat transfer coefficients in the nanowire-coated channels were typically higher compared to the plain channels. This disparity was attributed to dryout phenomenon in the channels during annular flow. Due to higher bubble generation activity in the coated channels, annular flow was induced earlier in the nanowire-coated array. At a given heat flux, higher mass fluxes are able to replenish the annular liquid film, thus preventing dryout on the channel walls. However, at low mass fluxes, the earlier transition to annular flow and the lower ability to replenish the liquid film on the channel walls induced dryout, thereby reducing heat transfer coefficients in the coated channels compared to the plain channels.

In summary, several issues in flow boiling relating to boiling incipience may be mitigated by engineering cavities on boiling surfaces, which should be optimised to within the active nucleation range using nucleation models such as the one proposed by Hsu [13]. Working fluid and operating conditions of the heat sink, in particular, system pressure and degree of subcooling have a notable effect on the active nucleation range. Enhancement in two-phase heat transfer may be obtained through an increase in nucleation site density, as well as improved wettability, where the latter appears to be more effective for water rather than wetting fluids like refrigerants. Porous coatings, amongst other surface enhancement techniques, are cost effective and more readily applied to machined microchannel heat sinks. However, further work to validate and improve the durability of some coatings is of paramount importance in ensuring consistent heat transfer performance. Notably, the operating conditions of heat sinks should also be considered when employing surface coatings, as it has been shown to have a significant impact on heat transfer enhancement. Porous coatings are typically reported to be effective where nucleate boiling is active (i.e. low vapour quality), but are generally less effective in flow regimes where convective boiling is dominant. As operating conditions such as heat flux and mass flux have a significant effect on flow pattern development in microchannels, these parameters should also be investigated to assess their respective effects on enhancement trend. Importantly, all enhancement effects in heat transfer should be weighed against the pressure drop penalty incurred by the coating in order to justify a higher yield in cooling performance over system power consumption.

In this study, a porous coating is applied to a copper microchannel heat sink with 44 channels, produced by computerised numerical control (CNC) micro-milling. The coating was applied on all three heated walls of the channels. The nanoFLUX® coating is a proprietary coating provided by Oxford nanoSystems Ltd consisting of a metallic (copper nickel alloy) dendritic nano- and microstructure, allowing for optimisable porosity and cavity size distribution

for bubble nucleation. Oxford nanoSystems Ltd has been optimising the structure for different refrigerants in the HVAC sectors. The use of HFE-7200 is a refrigerant not previously tested and so a deposition time (that could normally vary from 10 to 180 minutes) was chosen based on past experience with other refrigerants to give a dendritic structure of around 10 microns allowing also for the fact the coating was being integrated into very small microchannels. The thickness of the coating applied at the bottom and side walls of the microchannels was between 5 – 10 μm thick. The coating was demonstrated to perform without any degradation in tests similar to the ones described in this paper.

The flow boiling behaviour of dielectric fluid HFE-7200 in a conventional CNC-milled copper microchannel heat sink is compared against the coated sample of a similar configuration under the same operating conditions. The inlet pressure and degree of subcooling were fixed at 1 bar and 10 K respectively. The range of wall heat fluxes studied was between 24.5 kW/m^2 to 234.3 kW/m^2 while the mass fluxes investigated ranged from 200 kg/m^{2}s to 400 kg/m^{2}s.

2. Experimental methodology

The experimental facility has been described in detail in [25] and is depicted in Fig. 1. The working fluid, HFE-7200, flows in the main loop, which includes the test section, air-cooled condenser, micro-gear pump and two Coriolis mass flowmeters, each used for different ranges to measure flow rate. A water-glycol chiller in the auxiliary loop is used to regulate fluid temperature in order to preserve proper operation of the gear pump. A pre-heater controlled using a variac is located just before the test section to regulate the inlet temperature of the microchannel heat sink. As dissolved air may affect the experimental measurements, the working fluid was boiled in the reservoir and degassed through a valve at the start of each set of experiments. A detailed schematic of the test section is provided in Fig. 2. The copper microchannel evaporator has forty-four channels (i.e. number of channels, N, is 44) of width, W_{ch} = 0.36 mm, height, H_{ch} = 0.7 mm and length, L_{ch} = 20 mm, milled with a wall thickness of 0.1 mm on a 20 × 20 mm square area on the top of the copper block (D_h = 475 μm, fin thickness, W_f, is 0.1 mm). The coated copper microchannels have similar dimensional values, with a slightly smaller hydraulic diameter, i.e. D_h ~ 456 μm, as a result of the coating (coating thickness ~ 5 – 10 μm). Five thermocouples were embedded in the block along the centre of the channels and 1.6 mm from the bottom surface at the dimensionless axial positions: z/L = 0.17, 0.34, 0.5, 0.67 and 0.83 to help measure the local heat transfer coefficient. The inlet/outlet temperature and heat sink pressure drop are measured at the fluid line in the top plate. A differential pressure transducer with a range of up to 2.1 bar is used to measure pressure drop across the heat sink. Flow visualisation was conducted along the channel at the centre of the heat sink as illustrated in Fig. 2 at a resolution of 512 × 512 pixels and 5000 fps for a duration of 1.3 s. Camera locations 1, 2, 3 and 4 refer to specific positions along the channels, which are the channel inlet, first centre, second centre and channel outlet. Each photograph covers a distance of 4.4 mm.

2.1. Data reduction

The local heat transfer coefficient, $h_{(z)}$, is calculated as in Eq. (1), where $T_{f(z)}$ is the local fluid temperature, evaluated based on energy balance if in single-phase flow. The subcooled length, L_{sub}, was obtained based on the iterative method detailed in [25]. In the flow boiling region, $T_{f(z)}$ is the saturation temperature evaluated at the local saturation pressure based on a linear pressure drop assumption, see [25]. The base heat flux q''_b was calculated by obtaining the temperature gradient using temperatures
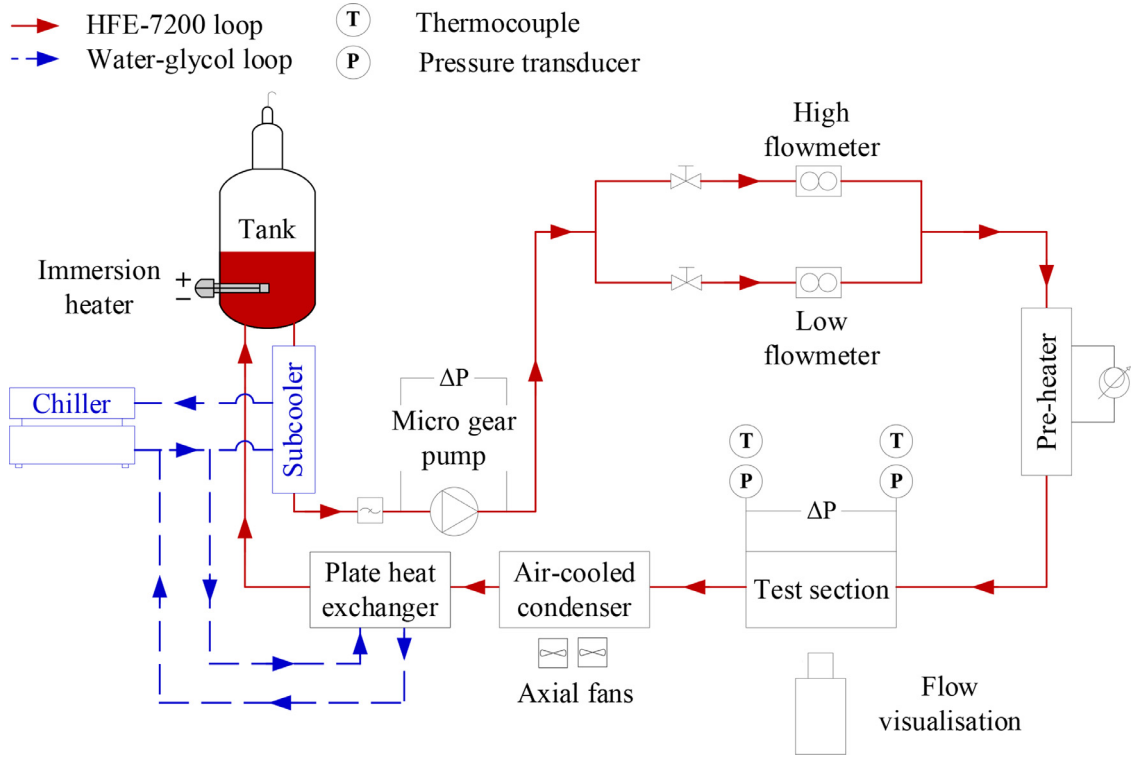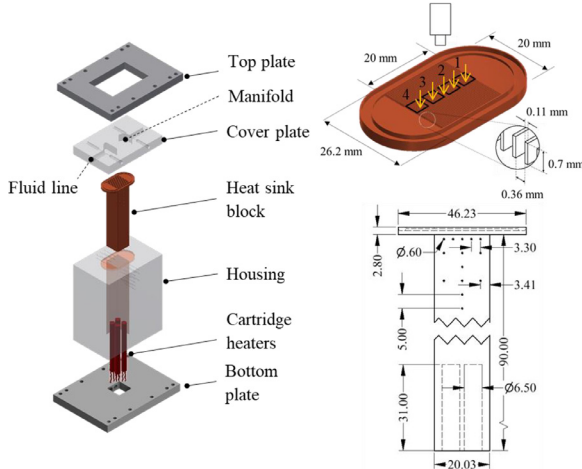
Fig. 1. Experimental flow loop [25].

Fig. 2. Test section details [25].

recorded by six thermocouples in the vertical direction. $T_{w(z)}$ is extrapolated from the five axial thermocouple readings assuming 1D conduction. W_f, W_{ch}, H_{ch} and η are the fin width, channel width, channel height and fin efficiency respectively. The fin efficiency is calculated assuming an adiabatic tip [26]. Further details of the data reduction procedure, including steps used to obtain the single-phase friction factor, Nusselt number, channel pressure drop and details of the test facility can be found in [25].

$$h_{(z)} = \frac{q''_b (W_{ch} + W_f)}{\left(T_{w(z)} - T_{f(z)}\right)(W_{ch} + 2\eta H_{ch})} \tag{1}$$

The average two-phase heat transfer coefficient, $\bar{h}_{tp}$, is obtained over the saturated length of the channel, which may be estimated by $L_{sat} = L_{ch} - L_{sub}$. The procedure to calculate L_{sub} is given in [25].

$$\bar{h}_{tp} = \frac{1}{L_{sat}} \int_{L_{sub}}^{L_{ch}} h_{(z)} dz \tag{2}$$

The percentage of heat transfer enhancement, E_{ht}, is calculated using the following equation:

$$E_{ht\%} = \frac{\bar{h}_{tp,coated} - \bar{h}_{tp,plain}}{\bar{h}_{tp,plain}} \times 100\% \tag{3}$$

The pressure drop in the microchannel array is as follows:

$$\Delta P_{ch} = \Delta P_{meas} - \Delta P_{loss} \tag{4}$$

where ΔP_{meas} is the measured pressure drop and ΔP_{loss} is the pressure loss in the manifolds, which may be up to 32% of the total measured pressure drop across the heat sink. The procedure to calculate ΔP_{loss} is given in [25]. Two-phase pressure drop in the channels is thus obtained by isolating the total pressure drop in the microchannel array from the single-phase component, ΔP_{sp}, based on the subcooled length at each operating condition.

$$\Delta P_{tp} = \Delta P_{ch} - \Delta P_{sp} \tag{5}$$

Pressure drop in the single-phase region is calculated based on the single-phase friction factor evaluated using the relation proposed by Shah and London [27] for developing flows, which takes into account the aspect ratio of rectangular channels.

The pressure drop penalty imposed by the coating is evaluated based on Eq. (6):

$$\Delta P_{pen} = \frac{P_{tp,coated} - P_{tp,plain}}{P_{tp,plain}} \times 100\% \tag{6}$$

where $\Delta P_{tp,plain}$ and $\Delta P_{tp,coated}$ are the two-phase pressure drop in the plain and coated channels respectively.

Data was acquired at a frequency of 1 kHz and for a period of 90 seconds when all readings are in quasi steady-state conditions and do not vary in trend. Quasi steady-state is defined when
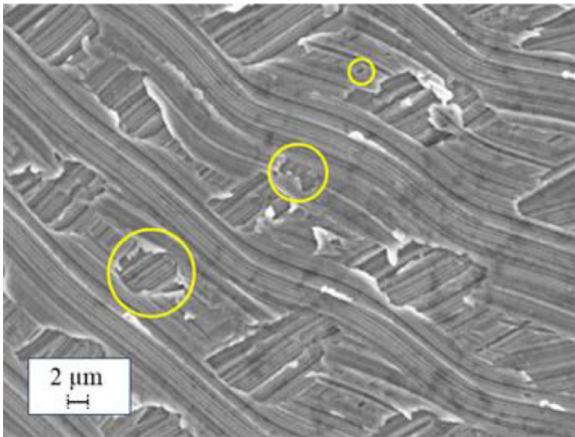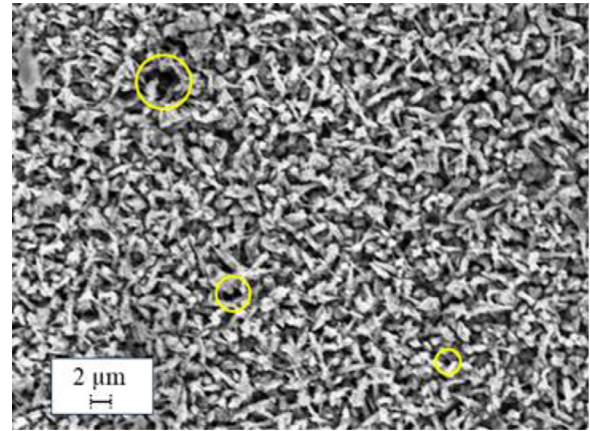
Fig. 3. Surface structure of the plain channel.

Fig. 4. Surface structure of the coated channel.

the fluctuations are within ±0.2 g/s for mass flow rate, ±0.5 K for inlet/outlet temperature and ±0.05 bar for the inlet/outlet pressure over a period of at least 180 s. Live flow visualisation was also used to assess steady flow before data acquisition. Scanning Electron Microscope analysis was conducted on the LEO 1455VP at the Experimental Techniques Centre in Brunel University London. The propagated experimental uncertainties were evaluated based on the method described in Coleman and Steele [28]. The maximum uncertainty values of single-phase friction factor, single-phase Nusselt number, wall heat flux, two-phase heat transfer coefficient and vapour quality for the current experimental range are $\pm2.5\%$, $\pm12.8\%$, $\pm9\%$, $\pm10.4\%$ and $\pm10\%$ respectively. Single-phase validation was conducted to verify the measuring instruments and data reduction method applied. Furthermore, the reproducibility of the experimental data was assessed and discussed in detail in [25]. For the results presented in the current study, the reproducibility of the heat transfer coefficient in the plain and coated channels exhibited a maximum mean absolute value of $\pm2.9\%$ and $\pm2.7\%$ respectively. The results of the plain channels as well as the relevant properties have previously been reported in [25].

3. Surface characterisation

Surface characteristics, fluid properties and operating parameters such as system pressure influence significantly the bubble nucleation process on boiling surfaces, see Mahmoud and Karayiannis [2]. Two-phase flow pattern development and flow boiling behaviour in microchannel systems are inevitably dependent on bubble nucleation, generation frequency and bubble dynamics. Since the working fluid and operating conditions were kept constant in both test sections, the primary difference in bubble generation frequency is likely to be caused by the difference in surface structure of the two test sections. The surface topography of the CNC micro-milled plain copper microchannels and the nanocoated microchannels were analysed using SEM in order to achieve a better understanding of the physics behind the effects of nanocoating on flow boiling results compared to the baseline plain microchannel results. The coating was applied on the bottom and side walls of the channel on the heat sink. The plenum areas were masked and are not coated.

Figs. 3 and 4 depict the surface characteristics of the channel bottom wall at a magnification of 5000x as measured on the plain and coated channels respectively. Examples of potential bubble nucleation sites are marked on each image. Potential nucleation sites were determined using ImageJ through image thresholding. Surface defects produced by feed marks, smeared material and metal debris during the micro-milling process result in cavities that could

potentially support bubble nucleation with sufficient surface superheat. On the contrary, a uniform layer of dendrite structures deposited in random orientations produce irregular pores that can potentially serve as nucleation sites on the coated surface. Cavities identified from the surface of the plain microchannel appear to be shallower, while cavities found on the coated surface are more defined and seem deeper in comparison. Generally, the plain microchannel surface was covered with cavities of widths between 6 – 10 μm. However, a few small cavities, ~ 0.7 μm in size, have also been identified. On the other hand, the treated surface was much more densely populated with small and medium size cavities with widths ranging from 0.6 to 3.3 μm. It can be concluded that there is an abundance of potential nucleation sites in the coated microchannels compared to the plain, CNC-milled microchannels. In addition, the cavities in the coated test section are more defined compared to the surface defects on the plain microchannels.

A nominal square area of 35 μm x 35 μm was selected from Fig. 3 and Fig. 4 to conduct an analysis of the cavity radius sizes found on the surfaces using ImageJ [29]. The radius of the cavities was approximated by assuming a circular area, using the area of the cavities identified by the software and an example is shown for the coated channel in Fig. 5. The distribution and number of cavities identified on each surface are superimposed on a plot of Hsu's predicted active nucleation range for HFE-7200 and operating conditions of P = 1 bar and ΔT_{sub} = 10 K for a hydraulic diameter of 475 μm, see Fig. 6. Note that the curve corresponds to the bottom axes (i.e. Wall Superheat [K]) while the bars correspond to the top axes (i.e. Number of cavities [-]). Importantly, the plots illustrate that the cavities observed on both surfaces are within the active nucleation range for the working fluid.

From Fig. 6, it is clear that the coatings provide cavities in the smaller range for nucleation. It is also clear that the number of cavities available on the coated surface is substantially higher compared to the plain surface. For instance, both surfaces are populated with cavities between 0.25 μm and 4.5 μm, which would be activated with wall superheat degrees of 1 K to 4.5 K on the surface. There are 15 and 361 cavities on the plain and coated surface respectively within this range, in other words, the number of cavities on the coated surface was 32 times higher than on the plain surface. Furthermore, as mentioned above, the deeper cavities may encourage vapour entrapment on the coated surface.

The contact angle of HFE-7200 on a copper surface was measured on a separate flat copper sample using the static sessile droplet method at atmospheric conditions using an in-house contact angle goniometer setup, which includes high speed video imaging [29]. The coating had a minimal effect on the contact angle of HFE-7200, which is by nature a wetting fluid. The contact
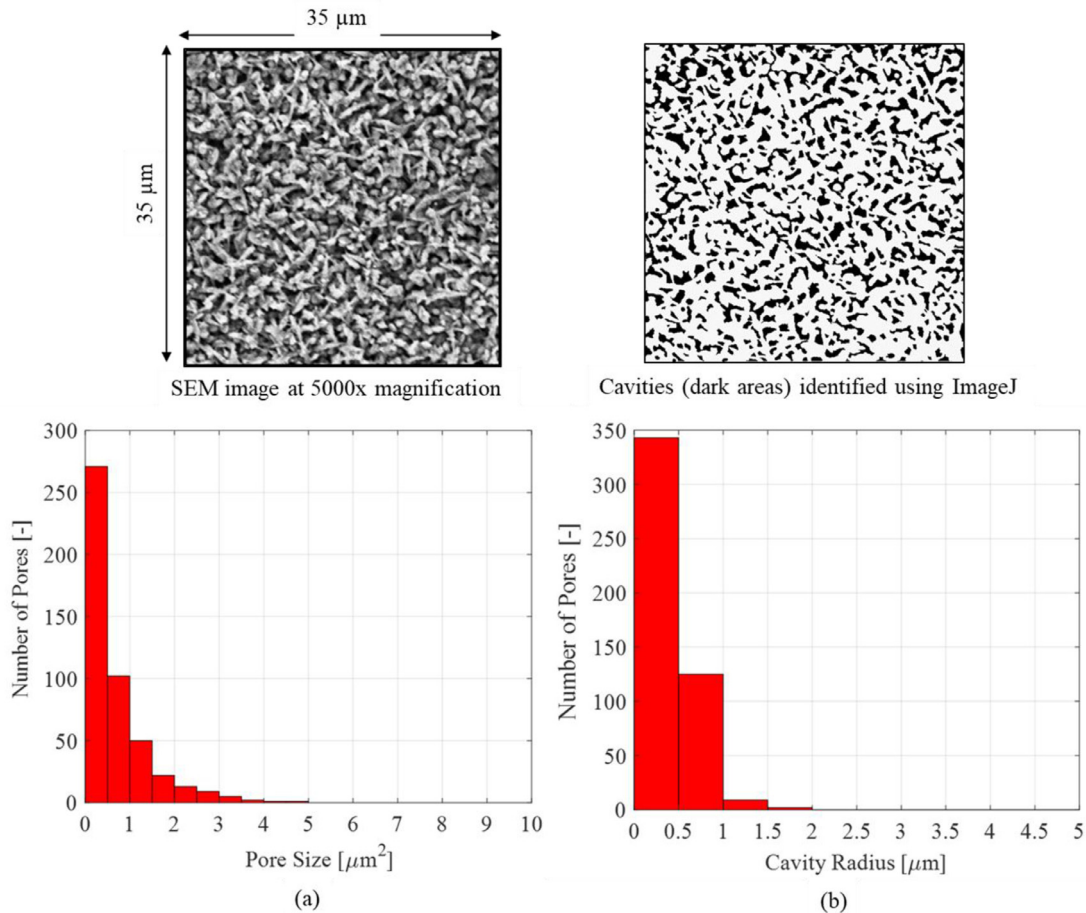
Fig. 5. Results from image analysis on the coated channel, showing (a) the distribution of pore area and (b) the distribution of cavity radius on the surface.

angles of HFE-7200 were around 12° on the plain and coated surface.

4. Results and discussions

4.1. Single-phase validation

Single-phase adiabatic and heat transfer experiments were conducted in both test sections to validate the instruments used in the test facility. Whilst the single-phase results of the coated channels may not be directly comparable to correlations, these have been included to discuss indicative results between the plain and coated test sections in single-phase mode. The friction factor is plotted against Reynolds number in Fig. 7 and the experimental Nusselt number is shown as a function of Reynolds number in Fig. 8. For the adiabatic tests, the mass flux was varied from G = 250 – 2250 kg/m^{2}s at inlet pressure and temperature of P = 1 bar and T = 40 °C. For the diabatic tests, a base heat flux of q$_b''$ ~ 5 kW/m^2 was applied across the same range of mass fluxes under similar operating conditions.

As mentioned above, the hydraulic diameter considered for the plain and coated channels are 475 μm and 455 μm respectively. The experimental results appear to be in good agreement with established prediction correlations summarized in Shah and London [27], Peng and Peterson [30] and Stephan and Preusser [31]. The single-phase friction factor obtained experimentally in the coated channels was relatively close to the correlation of Shah and London [27] for developing flows in conventional rectangular channels at Re < 500 and begins to diverge from the correlation at Re > 500.

This may be attributed to higher frictional losses generated due to local turbulence brought about by the rough structure of the coated channel walls, which is clearly illustrated in Fig. 4. Details of the correlations employed and their applicability to the current study are given in [25].

The friction factor and Nusselt number in the coated microchannel test section is higher than that of the plain test section. This may be attributed to the surface coating creating additional resistance to flow, increasing pressure drop in the channels. The higher experimental Nusselt number is a result of the enhanced single-phase heat transfer rates in the coated test section, which may have been promoted due to increased surface area and increased local mixing by the coated surface.

4.2. Flow patterns

Flow visualisation was conducted at four locations along the channel array to capture flow pattern evolution corresponding to each heat flux condition. High-speed recordings were conducted at 5000 fps and resolution of 512 × 512 pixels for a duration of 1.3 s at each location (see Fig. 2 for the locations). It is important to note that the high-speed recordings are not simultaneous. Flow visualisation was conducted when there are no significant changes in the measurements and flow pattern is observed to be quasi-steady. Hence the flow patterns captured, although not simultaneously at each location, remain a good representation of the flow pattern development along the channels. This was also verified by repeating the observations at two different occasions. Flow patterns observed in this study were categorised into bubbly, slug, churn and annu-
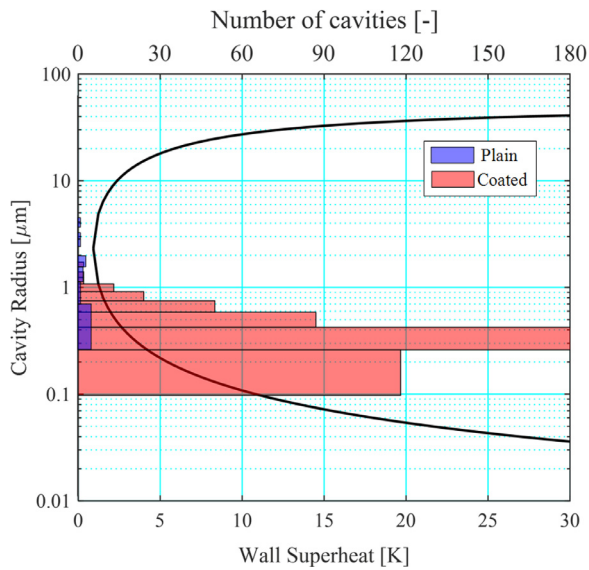
Fig. 6. Comparison of surface cavities on the plain and coated channel with the active cavity range predicted using Hsu's model at P = 1 bar and $\Delta T_{sub} = 10$ K for HFE7200. The curves correspond to the bottom axes (i.e. Wall Superheat [K]) while the bars correspond to the top axes (i.e. Number of cavities [-]). The area measured is 35 μm x 35μm.

Fig. 7. Friction factor vs. Reynolds number.
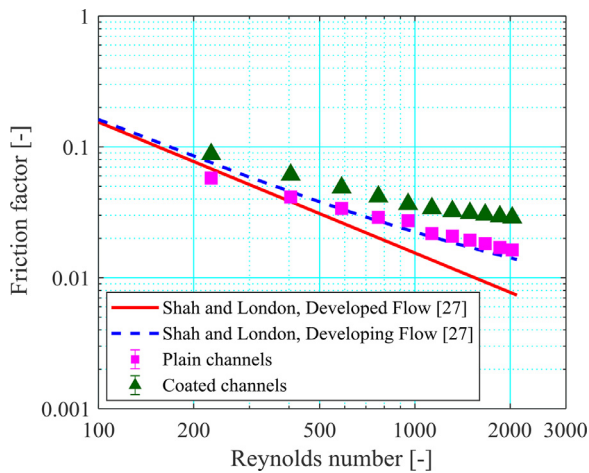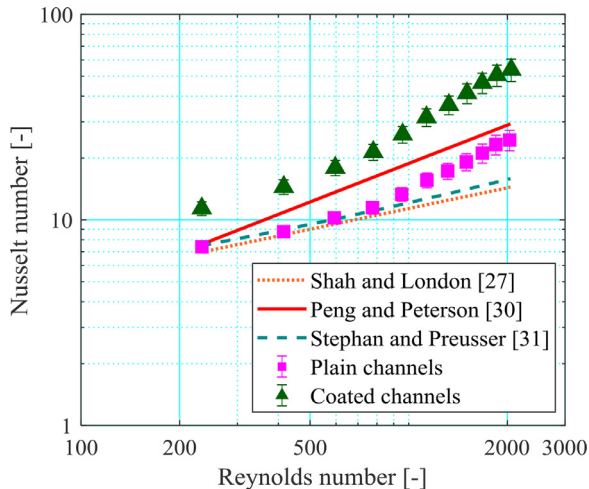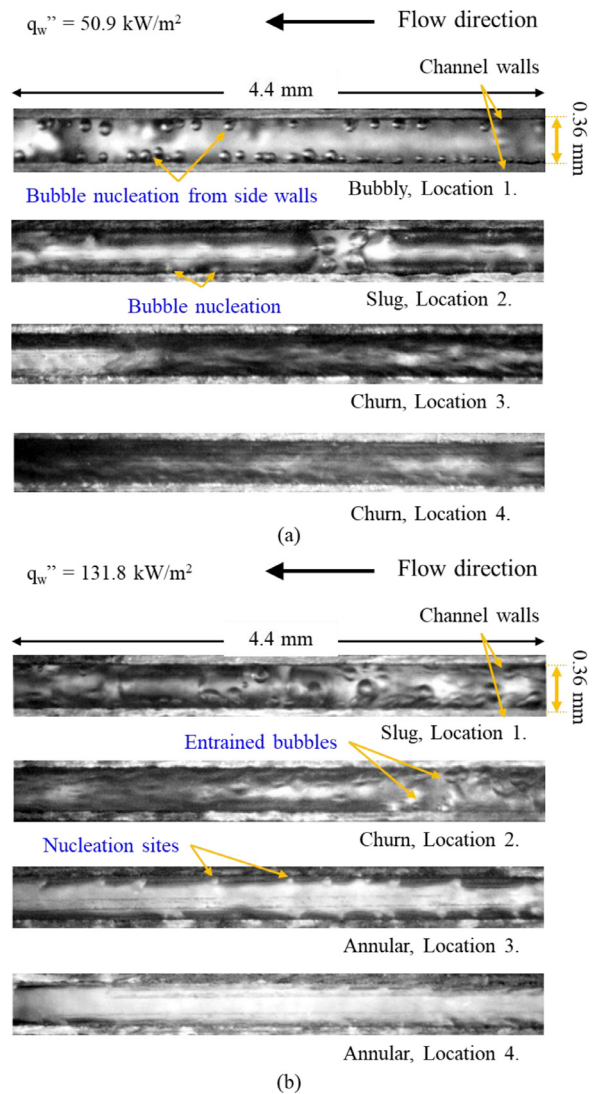

Fig. 8. Nusselt number vs. Reynolds number.

Fig. 9. Flow patterns in the plain microchannels at (a) $q_w'' = 50.9$ kW/m^2 (i.e. x = 0.01 to 0.17) and (b) $q_w'' = 131.8$ kW/m^2 (i.e. x = 0.04 to 0.50), G=200 kg/m^{2}s (Locations depicted in Fig. 2).

lar flow. The method of classification of flow regimes have been presented in [25]. As a result of the layer of coating on the top of the fins, there was some fluid transfer over the tops of fins as the top plate was not able to seal sufficiently. Nonetheless the flow pattern development in the channels was not significantly affected and was mainly influenced by bubble ebullition and flow dynamics in the two-phase process. The layer of coating is ~ 5 – 10 μm in thickness. Therefore, the fins of the coated channels appear thicker compared to the plain channels. However, there is only a maximum of 4% difference in hydraulic diameter between both test sections and the results thus remain comparable in the scope of this study. Photographs of flow regimes captured along the channel at the centre of the heat sink at P = 1 bar, G = 200kg/m^{2}s and $\Delta T_{sub} = 10$ K are shown in Fig. 9 at q_w" = 50.9 kW/m^2 and q_w" = 131.8 kW/m^2 for the plain channels and in Fig. 10 at q_w" = 50.4 kW/m^2 and q_w" = 125.2 kW/m^2 for the coated channels.

With increasing heat flux and vapour quality, the two-phase flow pattern developed from bubbly to slug, churn and annular flow in the streamwise direction. Bubbly flow occurs at very low heat fluxes just after the onset of boiling in the channels. It is characterised by small nucleating bubbles (Bubbly, Location 1, Fig. 9(a))
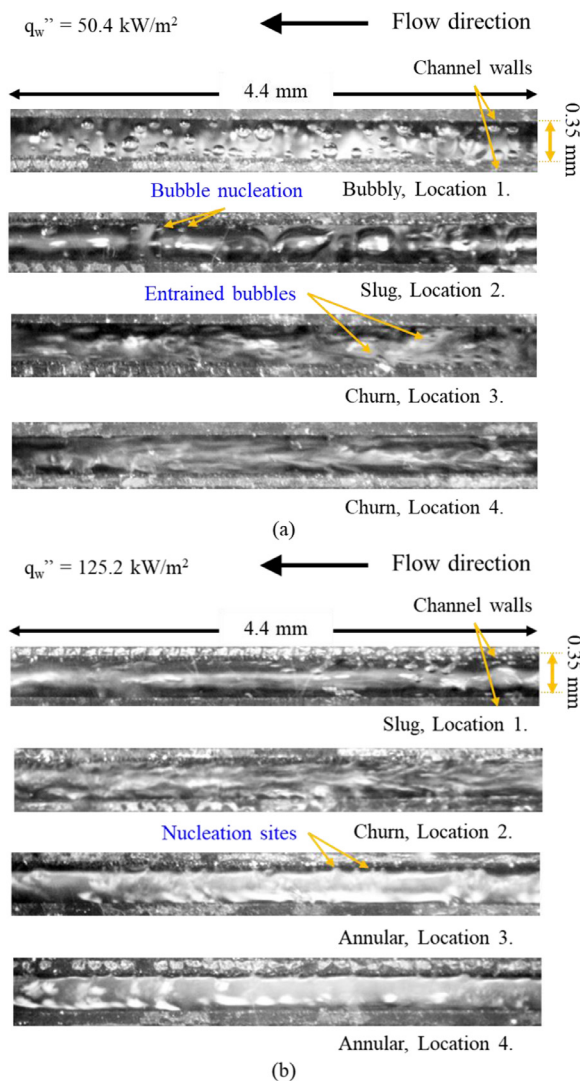
Fig. 10. Flow patterns in the coated microchannels at (a) $q_w^{''}$ = 50.4 kW/m^2 (i.e. x = 0.01 to 0.17) and (b) $q_w^{''}$ = 125.2 kW/m^2 (i.e. x = 0.03 to 0.56), G= 200 kg/m^{2}s (Locations depicted in Fig. 2).

Table 1

Flow pattern transition vapour qualities in the plain and coated heat sink at P = 1 bar, G = 200 kg/m^{2}s and ΔT_{sub} = 10 K for wall heat fluxes ranging from $q_w^{''}$ = 24.5 – 160.7 kW/m^2. (B-S: Bubbly to Slug; S-C: Slug to Churn; C-A: Churn to Annular)

Test section	x_{B-S} [-]	x_{S-C} [-]	x_{C-A} [-]
Plain	0.037	0.068	0.30
Coated	0.008	0.067	0.30

sites seem to be suppressed periodically in-phase with the intermittent and dispersed-phase churn wave. The churn regime captured in Fig. 9(b) (Churn, Location 2) and Fig. 10(a) (Churn, Location 3) show entrained vapour bubbles within the dispersed churn wave, which could have come from bubbles being stripped from their respective nucleation sites and entrained in the mixture as each wave accelerates downstream.

Annular flow develops after churn flow in the channels. This is characterised by a thin liquid film attached to the channel side walls with a vapour core in the middle of the channel. As mentioned above, long slugs have also been observed in the slug flow regime. The distinction between slug and annular flow is the observation of isolated slugs in the interim between subsequent long slugs in slug flow and an uninterrupted vapour core in annular flow. Nucleation sites on the side walls remained active within the liquid film, as evident from Fig. 9(b) (Annular, Location 3) in the plain channel and Fig. 10(b) (Annular, Location 3) in the coated channel, but become suppressed with gradual thinning of the liquid film. Nucleation in the thin liquid film of annular flow was also reported by Borhani and Thome [32], Balasubramanian and Kandlikar [33], Al-Zaidi et al. [34] and more recently in Lee and Karayiannis [25]. As the layer is nearly depleted, the dispersed phase brought about by the intermittent churn flow rewets the channel walls and re-establishes a thin-liquid film on the channels. The annular liquid film in the coated channels exhibits a more irregular form.

Increasing mass flux from G = 200 kg/m^{2}s to 400 kg/m^{2}s at similar experimental conditions, i.e. inlet subcooling and system pressure up to exit vapour qualities near to 1, accelerated flow regime transition from bubbly to slug, churn and annular flow in the plain heat sink. This may be attributed to increased rate of bubble coalescence with higher flow inertia at higher channel mass fluxes, triggering earlier transition from bubbly to slug flow in the channels. At the lowest mass flux, bubbly-slug transition occurred at x = 0.04 while at the higher mass fluxes, slug flow developed at very low vapour qualities of x < 0.01. The higher flow inertia may also have encouraged the establishment of a clear vapour core characteristic of annular flow in the channels, thus inducing earlier annular flow development in the channels at higher mass fluxes. Churn-annular transition occurred at x = 0.30, x = 0.20 and x = 0.17 at mass fluxes G = 200, 300 and 400 kg/m^{2}s respectively.

4.2.1. Effect of porous coating

Overall, the flow pattern transition boundary for bubbly to slug flow shifted to lower vapour qualities in the coated test section for a similar wall heat flux range compared to the plain channels, see Table 1. Bubbly-slug flow transition occurred at x = 0.04 and x = 0.01 in the plain and coated test section respectively. This could be due to higher bubble nucleation activity in the coated channels, as highlighted in Section 4.2.

On the other hand, there was only a small disparity between the flow transition boundaries of slug-churn and churn-annular flow. Slug-churn transition occurred at x = 0.068 and x = 0.067 in the plain and coated channel respectively, while churn-annular transition occurred at a similar vapour quality of x = 0.3 in both test sections. Although high bubble generation activity induces ear-

and isolated bubbles flowing within the bulk flow. Comparing the bubbly flow regime in the plain and coated channel, bubble nucleation is more active in the coated channels in this regime, as evident from the higher density of bubbles observed at Fig. 10(a) (Bubbly, Location 1) compared to in the plain channel.

Slug flow occurs when the isolated bubbles grow to the size of the width of the channels and become confined. With further growth in size, the bubbles elongate to form slugs in the channels, some of which may expand up to the full length of the channel. Intense bubble nucleation activity also promotes the establishment of slug flow due to increased bubble coalescence in the channels. Slugs have been observed to suppress active nucleation sites in the channels and also to migrate from neighbouring channels via the inlet plena through flow reversal, as noted in a previous study [25]. However, the coated channels appeared to be less prone to nucleation site suppression as bubble nucleation activity and bubble generation frequency remained relatively high in the coated channels during slug suppression compared to the plain channels.

Churn flow occurs when the high velocity gas-phase within a slug forces the tip to collapse, breaking up individual slugs to form long slugs, with intermittent waves of a chaotic mixture of liquid and vapour accelerating toward the channel exit. Again, nucleation

lier transition from bubbly to slug flow, subsequent transitions from slug to churn and annular flow may be predominantly controlled by flow parameters such as mass flux and fluid properties such as vapour density.

As postulated in Section 4.2, the tips of individual slugs collapse when the superficial velocity of the vapour phase increases sufficiently and consequently induces transition to churn flow. Higher vapour phase flow velocity also promotes the development of a clear vapour core characteristic of annular flow in the channel, thus encouraging transition from churn to annular flow. Superficial gas velocity, given by the ratio of mass flux (G) and vapour quality (x) over gas density (ρ_g), i.e. Gx/ρ_g [35] and widely used as a flow pattern transition criterion for slug-churn as well as churn-annular boundaries [36], can thus be reasonably assumed as a controlling parameter in transition to churn and annular flow. Since the flow pattern visualisation data were obtained at similar mass flux, inlet pressure and subcooling conditions for both the plain and coated test section at comparable ranges of wall heat fluxes, the superficial gas velocities do not differ significantly at a nominal wall heat flux level. This could explain similar vapour qualities at slug-churn and churn-annular transition in both test sections, see Table 1. Notably, this indicates that for the current microchannel geometry and experimental range studied, transition to churn and annular flow is less influenced by bubble generation frequency, which as noted above, is significantly higher in the coated channels.

Increasing mass flux from G = 200 kg/m^{2}s to 400 kg/m^{2}s at similar experimental conditions, i.e. inlet subcooling and system pressure up to exit vapour qualities near to 1, accelerated flow regime transition from bubbly to slug, churn and annular flow in the plain heat sink. This may be attributed to increased rate of bubble coalescence with higher flow inertia at higher channel mass fluxes, triggering earlier transition from bubbly to slug flow in the channels. At the lowest mass flux, bubbly-slug transition occurred at x = 0.04 while at the higher mass fluxes, slug flow developed at very low vapour qualities of x < 0.01. The higher flow inertia may also have encouraged the establishment of a clear vapour core characteristic of annular flow in the channels, thus inducing earlier annular flow development in the channels at higher mass fluxes. Churn-annular transition occurred at x = 0.30, x = 0.20 and x = 0.17 at mass fluxes G = 200, 300 and 400 kg/m^{2}s respectively.

Coating-induced acceleration of flow regime transitions was much less apparent at higher mass fluxes, potentially due to the effects of flow inertia, see Section 4.2. Importantly, increasing system mass flux appeared to mitigate cyclic dryout during the annular flow regime in the coated heat sink. For instance, dryout periods of around 30 ms in the coated heat sink were periodically observed during annular flow at $q_w^{"}$ = 153.3 kW/m^2 with a mass flux of G = 200 kg/m^{2}s. At higher mass fluxes of G = 300 kg/m^{2}s and 400 kg/m^{2}s, persistent wall dryout (i.e. < 1 ms) was not observed during annular flow in the coated heat sink. This is to say that wall dryout during annular flow was rewetted almost immediately by the churn wave mechanism [25]. The higher flow inertia could have enhanced the liquid film rewetting capability and mitigated dryout due to excessive bubble nucleation activity during the annular flow regime in the coated heat sink.

4.3. Flow boiling heat transfer

4.3.1. Boiling curve

Experiments were conducted in both test sections at a similar range of wall heat fluxes, namely $q_w^{"}$ = 26.1 – 160.7 kW/m^2 in the plain microchannel test section and $q_w^{"}$ = 24.5 – 153.3 kW/m^2 in the coated microchannel test section to investigate the effect of the nanocoating on microchannel flow boiling heat transfer performance. The applied heat flux was increased gradually to result in an exit vapour quality range of 0 to 1. The experimental variables,
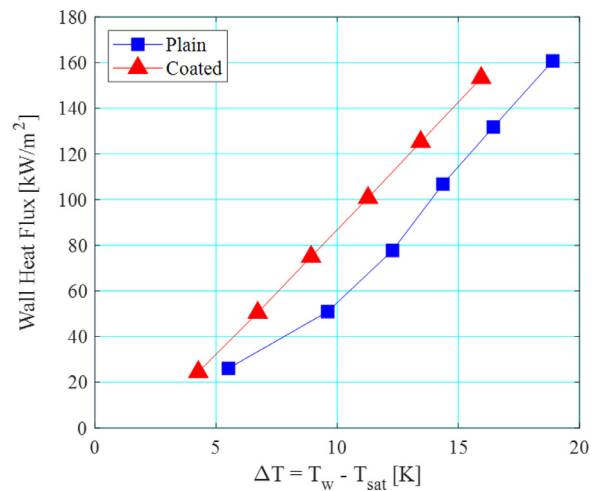

Fig. 11. Boiling curves of the plain and coated microchannel heat sink at the middle of the heat sink (i.e. z/L = 0.5) at P = 1 bar, G = 200 kg/m^{2}s and ΔT_{sub} = 10 K.

including mass flux, inlet subcooling and inlet pressure were kept constant at G = 200 kg/m^{2}s, ΔT_{sub} = 10 K and P = 1 bar.

The boiling curves at the dimensionless location of z/L = 0.5 (i.e. middle of the heat sink) in the plain and coated are depicted in Fig. 11. At a given wall heat flux condition, the wall superheat on the coated channels was on average 2.8 K smaller compared to the plain channels. For instance, at a wall heat flux of $q_w^{"}$ ~ 50 kW/m^2, wall superheat on the surface of the coated channels was 6.7 K, while on the plain channels the wall superheat measured was nearly 10 K. The lower degree of wall superheat on the enhanced microchannels could be due to the availability and activation of more nucleation sites within the activation range, as discussed in Section 3, provided by the coating. In practical terms, this means that for a given level of wall heat flux, the surface temperature of the heat sink, with the coating applied, will be around 3 K lower compared to the plain copper channels. Hence for a given junction temperature rating, the design heat flux may be higher using the coated heat sink. Since flow boiling experiments did not extend to wall superheats lower than 4 K, the effect of the porous coating on boiling incipience wall superheat is not apparent and thus not discussed in the current paper. Boiling hysteresis was not observed on both the plain and coated microchannels between wall heat fluxes of 20 kW/m^2 to 100 kW/m^2.

From Fig. 3 and Fig. 4, it is evident that the surface of the plain copper microchannels was characterised by relatively larger and shallower cavities in comparison to the topography of the coated microchannels. The characteristically deeper cavities of the coating may also encourage vapour trapping and increase bubble nucleation frequency. Furthermore, the coated surface has a substantially higher number of cavities available as nucleation sites compared to the plain channel, see Fig. 6. The higher nucleation activity (which contributes to higher nucleate boiling heat transfer coefficients) may explain the lower degree of wall superheat on the coated channel for a given wall heat flux.

4.3.2. Local heat transfer trend

As detailed above, local heat transfer coefficients are measured at five axial locations along the middle of the microchannel array in both test sections Figs. 12 and 13 present the measured local heat transfer coefficients along the length of the channel as a function of local vapour quality in the plain and coated microchannels respectively. The respective vapour qualities at which flow pattern transition occurs, indicating flow pattern development as described in Section 4.2, are annotated on the figures.
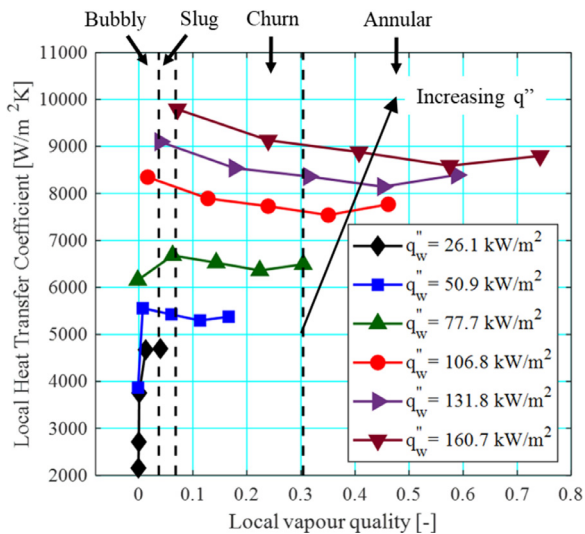
Fig. 12. Local heat transfer coefficient in the plain microchannels at a mass flux of 200 kg/m²s.

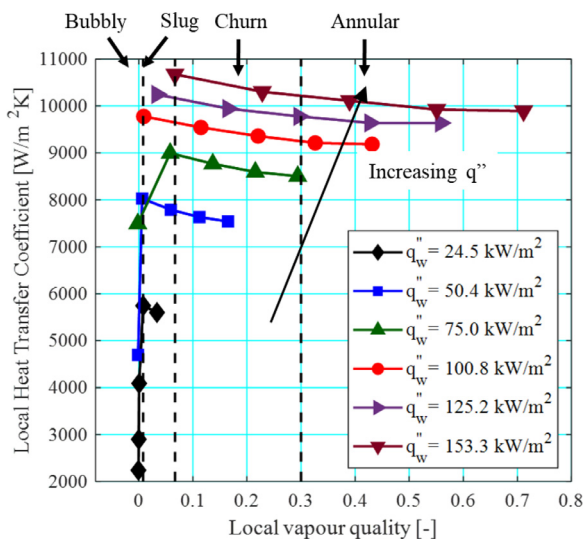**Fig. 13.** Local heat transfer coefficient in the coated microchannels at a mass flux of 200 kg/m²s.

Generally, there is a peak in local heat transfer coefficient just after the onset of boiling in the plain microchannels. The initial peak is followed by a decrease in local heat transfer coefficient with increasing vapour quality along the channel. Near the channel exit, there is a modest increase in heat transfer coefficient. Similarly, a peak in the local heat transfer trend is seen in the coated microchannels near the start of the saturated boiling region. Local heat transfer coefficient followed a slight decreasing trend along the channel thereafter. The local heat transfer trends in the plain channels have been reported in detail in [25]. Contrary to the observations made in the plain microchannel, the local heat transfer trend near the channel exit does not appear to increase in the coated microchannel test section.

The steep rise in heat transfer coefficient at low heat fluxes ($q_w'' = 26.1 – 50.9$ kW/m²), particularly in the subcooled region, is due to the change in main heat transfer mode from single-phase liquid convection to the more efficient nucleate boiling mode in the low vapour quality region where bubbly flow is observed. Subcooled boiling was observed in this study for both test sections. The peak is observed at low vapour qualities just after the onset

of boiling, in the region where bubble nucleation activity is very high, and thus the nucleate boiling mechanism can be reasonably assumed to dominate. A similar trend in the early stages of saturated flow boiling ($q_w'' = 24.5 – 50.4$ kW/m²) is also observed in the coated microchannels.

The subsequent decline in local heat transfer trend with respect to vapour quality observed in both test sections could be due to suppression of the high heat transfer rates associated with the nucleate boiling mechanism following flow pattern development into slug, churn and annular flow. This is supported by the flow visualisation results presented above, where it is noted that bubble nucleation activity in previously active sites were observed to be suppressed, possibly due to flooding of the cavities, especially in intermittent churn waves and periodic liquid film dryout in slug and annular flow. Additionally, the transient variation of local heat transfer coefficient at a fixed location in the channels following transition to slug flow could also have contributed to a drop in the time-averaged local heat transfer coefficient after the initial peak in heat transfer coefficient near the onset of boiling. Thome et al.'s three-zone model [37] predicts local heat transfer coefficients taking into consideration the periodic variation of heat transfer rates caused by (i) gradual thinning of the liquid film in slugs with film evaporation, (ii) local dryout following complete evaporation of the liquid film and (iii) the reinstatement of a liquid slug, which restarts the cycle of liquid film thinning, dryout and rewetting in the channels. Periodic dryout in the slug, churn and annular flow regimes were also observed in our flow visualisations and typically last ~ 100 ms. Although film evaporation rates increase with the thinning of the liquid film, relatively poor heat transfer coefficients are associated with the convective heat transfer occurring during the liquid slug stage and particularly in the dryout phase of the cycle. Oscillations in pressure drop readings corresponding to different flow phenomena have been extensively discussed in [25]. As a result, the time-averaged heat transfer coefficient at a particular location degrades after the onset of boiling and slug flow development due to bubble confinement and coagulation in the channels.

The increase in the heat transfer coefficient near the channel exit of the plain microchannel test section could be due to (i) thinning of the liquid layer and (ii) conjugate effects in the heat sink occurring at the boundaries between the microchannel array and the inlet and outlet plena, as explained in [25]. The less pronounced effect observed in Fig. 13 could be due to the augmented heat transfer coefficients obtained from the coated test section in comparison with the plain test section.

4.3.3. Average heat transfer coefficient

Overall, a clear increase in heat transfer coefficient with increase in wall heat flux can already be inferred from Fig. 12 and 13. To clarify the effect of wall heat flux on heat transfer coefficient in the plain and coated test section, the corresponding increase in average heat transfer coefficient (HTC) with respect to wall heat flux is plotted in Fig. 14. Two-phase heat transfer coefficient exhibits an ascending trend with increase in heat flux. Increasing wall heat flux increases wall superheat at the surface of the channels, which means that more potential nucleation sites may become activated. The correspondingly more vigorous bubble nucleation activity increases the average HTC value due to latent heat transfer and mixing currents induced by quenching at the wake of departing bubbles. Other than that, convective liquid film evaporation rate, which occurs around the perimeter of slugs and liquid films attached to the channel walls in churn and annular flow, may also increase with heat flux, see Thome and Consolini [38].

Importantly, the average HTC of the coated microchannel test section is superior to the heat transfer performance in the plain microchannels. Wall superheat was reduced by up to 3 K in the coated section for the current experimental range. The percentage
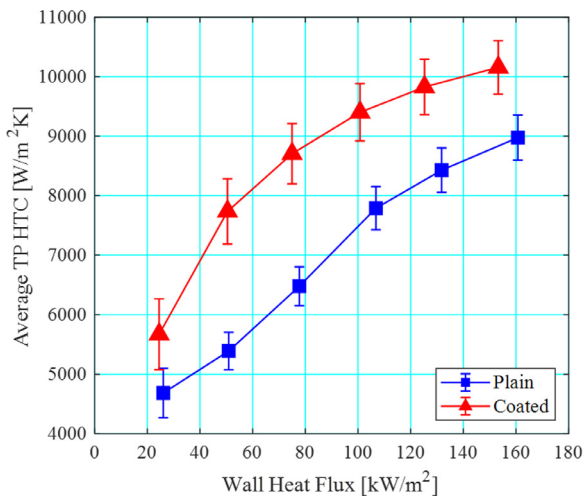
Fig. 14. Average two-phase heat transfer coefficient vs. wall heat flux in the plain and coated channels at a mass flux of 200 kg/m²s.
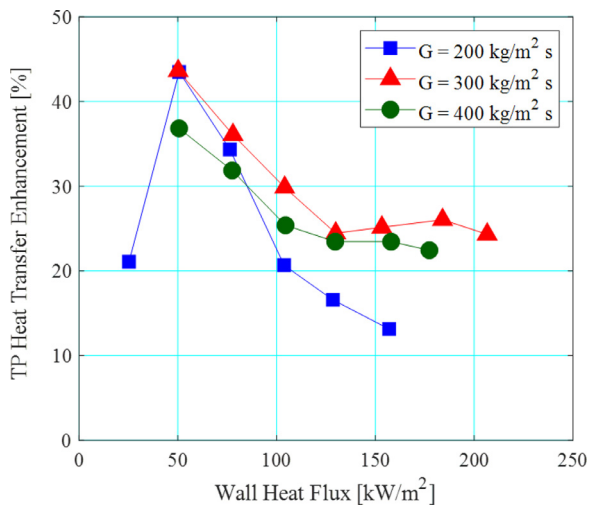

Fig. 15. Percentage enhancement in heat transfer at different mass fluxes with respect to wall heat flux, for operating conditions of P = 1 bar and ΔT_{sub} = 10 K.

of heat transfer enhancement relative to the plain microchannels (see Eq. (3)) is plotted in Fig. 15. The moderate HTC enhancement of 21.1% at the lowest heat flux ($q_w" \sim 25$ kW/m²), where bubbly flow was mainly observed and wall superheat was just above 4 K, could be due to the activation of few nucleation sites in both test sections at such a low superheat condition. The range of active nucleation sites increases with increasing wall superheat, based on the approximation provided by Hsu [13].

As the wall heat flux is increased to $q_w" \sim 51$ kW/m², wall superheat increases to around 7 K and a peak of 43.5% in heat transfer enhancement is recorded. At this heat flux, bubbly and slug flow were observed upstream, while churn flow developed downstream in both test sections. Notably, the bubbly flow regime occurred only very near the channel inlet of the coated test section, whereas bubbly flow persisted over a larger portion of the channels in the plain test section. It is clear from Fig. 3 and 4 that there is a larger number of cavities in the coated section, which are more defined compared to the surface defects seen on the bottom wall of the plain microchannels. Defined cavities may produce a stronger pinning effect on departing bubbles. This strong pinning effect may provide residual vapour pockets in the cavities from the preceding departing bubble, leaving behind a vapour embryo from which the subsequent bubble is able to grow from. This re-

duces the waiting time between subsequent bubble ebullition cycles, which could explain the higher bubble generation frequency in the coated channels and have been observed in our flow visualization, where higher bubble density in the channels were captured in the bubbly regime as shown in Fig. 10(a). Shallow surface cavities found on the plain microchannels may be less supportive for vapour entrapment, which increases waiting time (thus lowering bubble departure frequency) between subsequent bubble ebullition cycles in the plain microchannel test section. This is in addition to having a smaller number of cavities. As a direct consequence of higher bubble generation frequency and increased coalescence activity due to high bubble density in the coated microchannels, transition from bubbly to slug flow occurs at a much lower vapour quality in the coated test section than in the plain microchannel test section. Another possible enhancement effect could have resulted from the higher rate of heat transfer in the contact line between liquid slugs and the surfaces of the coated channels. Liquid film evaporation rate in the coated microchannels might have been promoted by increased wall turbulence with surface perturbations on the coated walls, postulated also as the reason for single-phase heat transfer enhancement.

Beyond $q_w" \sim 51$ kW/m², heat transfer enhancement degraded with increase in wall heat flux. A similar enhancement trend, that is, strong enhancement at the onset of boiling and depreciating enhancement with increase in vapour quality was also reported in Bai et al. [18]. Churn and annular flow dominate the flow pattern in the channels at moderate and high heat fluxes. As shown in the flow visualisation results, bubble nucleation activity appears to be suppressed intermittently in churn flow while nucleation sites in the liquid film of annular flow are also periodically suppressed with gradual thinning of the film. As a consequence, heat transfer augmentation, which appear to be stronger when bubble nucleation activity is relatively high, drops in the region where churn and annular flow become dominant. The stronger mixing currents within the liquid layer on the rough coated surface continue to support some amount of heat transfer augmentation, albeit weaker than the enhancement obtained in the bubbly flow region where nucleate boiling is the main contributor to heat transfer in the channels.

Fig. 15 also depicts the mass flux effect on percentage enhancements in average two-phase heat transfer. Wall heat flux ranged between $q_w" = 25.8$ and 206.6 kW/m². Note that at $q_w" \sim 26$ kW/m², flow boiling conditions are not yet established in the channels at G = 300 and 400 kg/m²s. Since the enhancement is specific to flow boiling heat transfer coefficients, values at the larger two mass fluxes have been omitted from the figure at this heat flux value. The uncertainty in this calculation ranged from ±1.3% to ±6.9%.

As covered above for G = 200 kg/m²s, the peak enhancement effect, which was attributed to the combination of an active nucleate boiling contribution and enhanced thin-film evaporation rates occurring from the slug liquid film, is typically obtained where the slug flow regime is dominant. A similar trend was observed for the higher mass fluxes. At G = 300 and 400 kg/m²s, the percentage enhancement peaked at $q_w" \sim 51$ kW/m², where slug flow was established in at least half of the full length of the microchannel array (i.e. 20 mm). The peak enhancement of 43.6% at G = 300 kg/m²s, was close to the value observed at G = 200 kg/m²s (i.e. 43.5%). At the highest mass flux condition of G = 400 kg/m²s, the maximum enhancement recorded was only 36.8% at a similar heat flux of $q_w" \sim 51$ kW/m². This could be due to the dominance of the flow inertia effect on the rate of bubble coalescence in the microchannels, which act to accelerate flow pattern development towards convective boiling dominant regimes and ultimately diminishes the enhancement effect in the microchannels at higher mass fluxes. As highlighted in Section 4.2.1, the smaller shift in flow pat-

tern boundaries also indicated a smaller coating effect on flow pattern transition boundaries at higher mass fluxes.

Contrary to the lowest mass flux condition, where the enhancement percentage decreased steeply with increasing heat flux between $q_w^{"} \sim 51$ to 104 kW/m^2, at higher mass fluxes of G = 300 and 400 kg/m^{2}s two-phase heat transfer augmentation depreciated sharply between $q_w^{"} \sim 51$ to 130 kW/m^2 but stabilised at around 25% with increasing heat flux beyond $q_w^{"} \sim 130$ kW/m^2. These heat fluxes correspond to the observation of the annular flow regime in at least half the total length of the channels (i.e. 20 mm). Furthermore, the percentage augmentation at G = 300 and 400 kg/m^{2}s is higher compared to the lowest mass flux condition of G = 200 kg/m^{2}s.

As highlighted in Section 4.3.2, bubble nucleation is periodically suppressed in the annular flow regime and thin-film evaporation contributes highly to two-phase heat transfer. The enhancement mechanism of the coating in thin-film evaporation may be partly attributed to the higher heat transfer area of the coated channels. However, higher evaporation rates also exacerbate wall dryout in the channels, especially during annular flow. The higher flow inertia at higher mass fluxes is able to replenish the annular liquid film at a higher rate than at lower mass fluxes. From flow visualisation, significantly shorter periods of dryout were also observed, as noted previously in Section 4.2.1. A similar mass flux effect was also observed in Li et al. [23] with a silicon nanowire coating, where water was used as a working fluid and two-phase heat transfer enhancement was only observed at higher mass fluxes (namely G > 238 kg/m^{2}s). Annular flow was prevalent in the channels and flow boiling heat transfer coefficients were found to be lower than in the plain channels at low mass fluxes due to wall dryout.

Notably, the enhancement percentages at G = 300 kg/m^{2}s is generally higher compared to G = 200 and 400 kg/m^{2}s. For the lowest mass flux condition, this may be attributed to dryout with increasing heat flux. Euh et al. [39] found that increasing mass velocity decreased bubble generation frequency from an active nucleation site. Steeper temperature gradients found on thinner thermal boundary layers at higher mass fluxes may result in longer waiting times to re-establish the wall superheat required to sustain bubble growth from a cavity. Whilst higher bubble generation frequencies may have resulted from the deeper cavities found on the coated surface, thus improving heat transfer coefficients in the coated channels, the high mass flux could have acted to subdue the high bubble generation frequencies from cavities of the coating. There is also a much earlier transition to the annular flow regime at G = 400 kg/m^{2}s, i.e. x = 0.15, which indicates a significantly earlier start on nucleate boiling suppression in the channels, decreasing the effect of the coating on heat transfer enhancement. Transition to annular flow only occurred at x = 0.3 and x = 0.19 at G = 200 kg/m^{2}s and 300 kg/m^{2}s respectively.

4.4. Flow boiling pressure drop

Pressure drop in the two-phase region of the channels is depicted in Fig. 16 for the plain and coated test section. In both heat sinks, two-phase pressure drop increases with increasing wall heat flux. This is mainly due to the effect of higher void fraction in the channels with increasing heat flux on the frictional and acceleration pressure drop components [25]. The difference in two-phase pressure drop between the plain and coated heat sink appears to increase with increasing wall heat flux. At a given wall heat flux condition, flow boiling pressure drop in the coated channels is higher in comparison to the plain channels. As highlighted in Section 4.2, higher bubble nucleation activity was observed in the coated microchannel heat sink. While the channel void fraction was not directly measured, the higher nucleation activity indicates higher void fraction in the coated channels. Accordingly, flow pat-
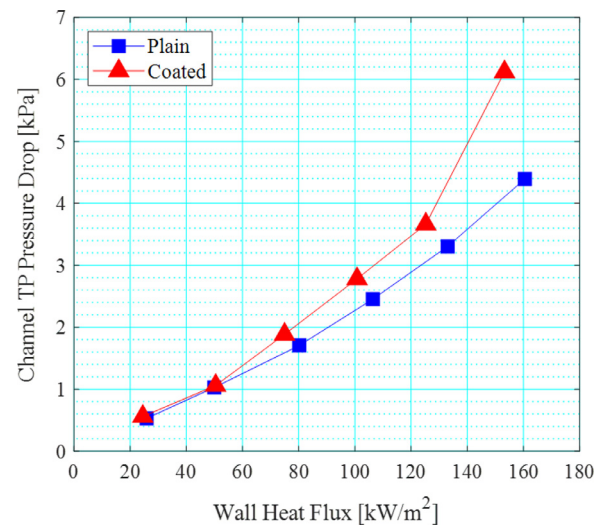

Fig. 16. Two-phase pressure drop in the plain and coated microchannels P = 1 bar, G = 200 kg/m^2 s and $\Delta T_{sub} = 10$ K.

tern transitions were also accelerated in the coated test section, especially the bubbly-slug transition boundary, see Table 1.

Notably, two-phase pressure drop in the coated heat sink rose significantly from 3.7 kPa to 6.1 kPa between wall heat fluxes $q_w^{"} = 125$ kW/m^2 and 153 kW/m^2. The region where annular flow is observed in the heat sink extended with the increase in wall heat flux, however, from flow visualisation and heat transfer coefficient trend, the critical heat flux limit was not reached at the highest wall heat flux condition in the coated heat sink. Interestingly, the magnitude of flow oscillations increased with the corresponding increase in wall heat flux. From Fig. 17, the standard deviation of the total pressure drop across the heat sink doubled from 0.05 kPa to 0.1 kPa between $q_w^{"} = 125$ kW/m^2 and 153 kW/m^2 in the coated microchannel test section. A possible relationship between pressure drop magnitude and oscillation has been suggested in [25] and should be subject to further study.

4.4.1. Pressure drop increase

To further investigate the increase in flow boiling pressure drop posed by the coating, the percentage difference in two-phase pressure drop between the plain and coated channels are calculated according to Eq. (6) and plotted in Fig. 18. The pressure drop penalty posed by the coating is shown to be highly dependent on wall heat flux. The uncertainty in the pressure drop penalty ranged from ±0.1% to ±0.2% for our examined conditions.

At G = 200 kg/m^{2}s and the lowest wall heat flux condition of $q_w^{"} = 25$ kW/m^2, flow boiling pressure drop in the coated heat sink was 5.5% higher in the coated heat sink compared to the plain heat sink. This is despite of the fact that slug flow has already developed in the coated microchannels at the lowest wall heat flux, while the two-phase flow pattern remained predominantly in the bubbly region in the plain heat sink (see Fig. 12 and 13). The relatively low percentage penalty could be due to the short two-phase length in the region (i.e. 8 mm) in the heat sink in relation to the total length of the channels (i.e. 20 mm). The coating had a smaller effect on slug-churn and churn-annular flow pattern transition boundaries in the microchannel heat sink (i.e. similar flow regimes were observed in both heat sinks at a given wall heat flux condition).

The two-phase pressure drop increase dropped slightly to 3.1% with increase in wall heat flux to $q_w^{"} = 51$ kW/m^2. This could be a result of smaller pressure drop oscillations in the coated heat sink, owing to lower wall superheat at the same heat flux condi-
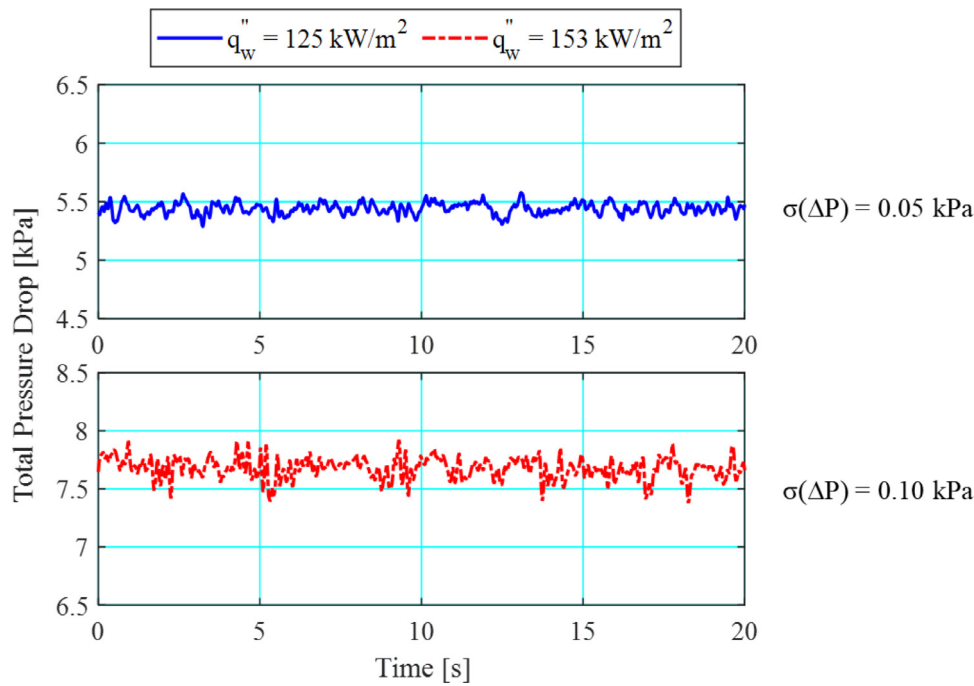
Fig. 17. Measured pressure drop across the coated heat sink at $q_w'' \sim 125$ kW/m^2 and $q_w'' \sim 153$ kW/m^2 over a window of 20 s for G = 200 kg/m^{2}s and ΔT_{sub} = 10 K.

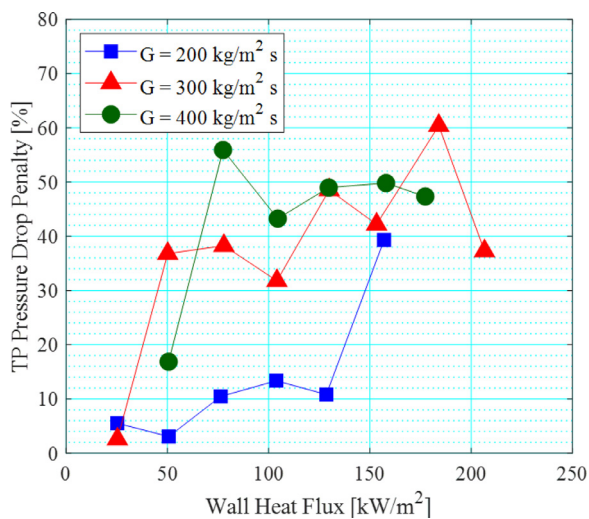**Fig. 18.** Two-phase pressure drop penalty as a result of the coating in the microchannel heat sink at P = 1 bar and ΔT_{sub} = 10 K at various mass flux conditions.

tion. Lower degree of superheat have been found to suppress rapid bubble growth instabilities near the onset of boiling. At this wall heat flux condition, bubbly flow is observed near the channel inlet of both heat sinks. The standard deviation in total pressure drop across the plain and coated heat sinks at q_w'' = 51 kW/m^2 were 0.55 kPa and 0.22 kPa respectively, seen in Fig. 19, while the coating lowered the wall superheat from 9.6 K to 6.8 K, see Fig. 11.

Following that, the flow boiling pressure drop increase due to the coating rose from 10.5% to 13.1% as churn and annular flow begins to dominate in the heat sink between q_w'' = 76 to 104 kW/m^2. The pressure drop penalty dropped slightly again to 10.8% at q_w'' = 128 kW/m^2 when annular flow was the dominant flow regime in both heat sinks. The relatively stable pressure drop penalty in this range of heat fluxes could be due to the fact

that similar flow regimes (mainly churn and annular flow) were observed in both heat sinks at a given wall heat flux condition, where the higher pressure drop could be induced by the slightly smaller hydraulic diameter of the coated channels and mainly the higher channel void fraction due to more active bubble nucleation in the coated heat sink. At the highest wall heat flux condition where annular flow was dominant in the coated microchannels, there was a large jump in the two-phase pressure drop penalty of almost 40%. This may be attributed to the sharp rise in channel two-phase pressure drop in the coated heat sink at q_w'' = 153 kW/m^2, as highlighted earlier from Fig. 19 and may be related to larger pressure drop oscillations in the heat sink.

Whilst the two-phase pressure drop penalty was as high as 84% in the coated test section at a lower subcooling degree of 5 K [29] due to the low flow rates employed and small pressure drop values observed in this study, the corresponding increase in power consumption across the heat sink is relatively small. Based on the pumping power consumption by the gear pump, the maximum power consumption in the coated heat sink was 1.7 W, which is only 0.2 W higher than the maximum power consumption of 1.5 W in the plain microchannel heat sink. Furthermore, the majority of the pressure losses in the system (thus also the power consumption) was found to be in fact in the experimental loop aside of the heat sink assembly [29], even though high pressure drop in microchannels is frequently cited as a limitation to two-phase cooling performance [40].

The pressure drop penalty imposed by the coating was generally higher at the two higher mass fluxes investigated. Additionally, the pressure drop penalty trend is much more erratic compared to G = 200 kg/m^{2}s. This could be related to the earlier dominance of annular flow at higher mass fluxes and the churn rewetting mechanism in the channels, which could result in upstream compressibility effects [41,42] and pressure oscillations. The large fluctuations in pressure drop increase at G = 300 kg/m^{2}s could be related to pressure oscillations in the heat sink.

Two-phase pressure drop penalty stabilised between 47.3% and 49.8% at G = 400 kg/m^{2}s in the wall heat flux range of q_w'' = 130
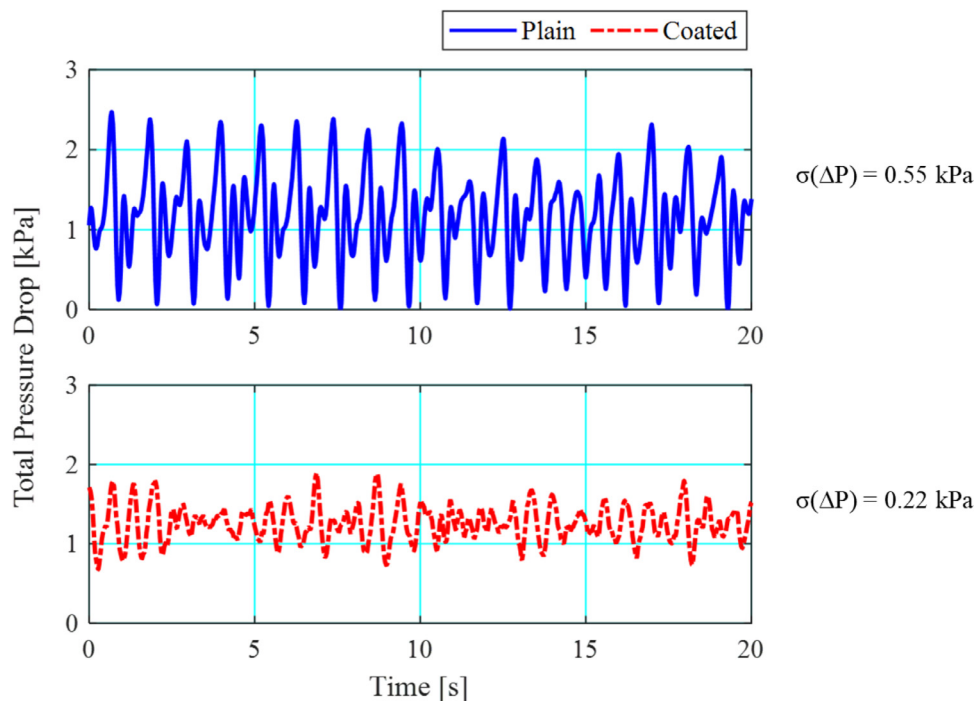
Fig. 19. Measured pressure drop across the plain and coated heat sink respectively at $q_w" \sim 51 kW/m^2$ over a window of 20 s for G = 200 kg/m²s and ΔT_{sub} = 10 K.

kW/m² and 177 kW/m². Incidentally at G = 400 kW/m², pressure drop oscillations decreased from 0.06 kPa to 0.04 kPa between $q_w" = 105$ kW/m² to 175 kW/m². As mentioned above, the dryout phenomenon and pressure drop oscillations in microchannel heat sinks have been found to be linked to pressure drop behaviour in microchannels [25]. Interestingly, dryout periods were relatively short at higher mass fluxes in the heat sink. This could suggest that the pressure drop oscillations are also coupled with the churn rewetting mechanism. Simultaneous flow visualisation and pressure drop measurements could be conducted to verify this effect.

5. Conclusions

Experimental flow boiling results using HFE-7200 in a plain and coated copper microchannel heat sink were presented and compared at operating conditions of P = 1 bar at the inlet, G = 200, 300 and 400 kg/m²s, fixed inlet subcooling of 10 K for heat fluxes ranging from $q_w" = 24.5$ to 234.3 kW/m². The corresponding heat flux based on the footprint area of the microchannel heat sink (20 mm x 20 mm) was 93.7 – 896.3 kW/m². Flow patterns observed in this study were bubbly, slug, churn and annular flow. Similar flow pattern trends were observed in both test sections, with an earlier transition from bubbly to slug flow in the coated microchannels. This is due to higher bubble generation frequency in the test section, which was confirmed by flow visualisation. SEM analysis demonstrated a higher density of potential nucleation sites available in the coated channels. Deeper cavities on the coated surface are believed to encourage vapour trapping, which results in lower waiting times between bubble ebullition cycles and thus increase bubble generation frequency. The churn and annular regime are more dependent on the superficial gas velocity and the coating had a less pronounced effect on all flow regime boundaries at higher mass flux.

Generally, local heat transfer coefficients peaked near the onset of flow boiling and decreased toward the channel exit. The peak in heat transfer coefficient just after the onset of boiling, where bubble nucleation activity is vigorous, is associated with high heat transfer rates in the nucleate boiling regime. The subsequent decrease in heat transfer coefficient may be attributed to increased nucleation site suppression and transient variations in heat transfer rate caused by dryout and rewetting cycles in the slug, churn and annular flow regimes. Average heat transfer coefficients increased with increase in heat flux, since more nucleation sites are activated in the channels with increasing wall superheat and liquid film evaporation rates become higher with increasing heat flux. Heat transfer enhancement was achieved using the coated microchannel heat sink, in the range investigated in this study. The enhancement peaked at 43.5% at $q_w" = 51.0$ kW/m² and dropped to 13.2% at the maximum heat flux studied. The enhancement effect was found to be stronger at heat flux levels where nucleate boiling has a large contribution to the overall heat transfer, owing to the significantly higher bubble nucleation activity in the coated channels. The convective boiling mechanism could also have been enhanced by increased wall turbulence and surface area brought about by the coating structure.

The enhancement was significant at all mass fluxes studied. However, heat transfer enhancement may be reduced at higher mass fluxes due to higher flow inertia and longer waiting times between bubble growth cycles. Mass flux was also found to affect the pressure drop increase due to the coating and this effect may be related to the churn wave rewetting mechanism.

The intricate relationship between the magnitude of pressure drop, oscillations and dryout is highlighted for further investigation using simultaneous flow visualisation and data acquisition.

Surface coating has been shown to be a promising technique to enhance flow boiling heat transfer rates in microchannels, especially if the flow boiling system is operating at nucleate boiling dominant regimes. Although pressure drop penalty may reach up to 60% in the coated heat sink, the relatively small pressure drop values (due to the short channel length and low flow rates employed) in the microchannel array demonstrated that the coating is a good method to enhance heat transfer rates in microchannels, as the pressure drop penalty incurred is insignificant in terms of total system power consumption.

Declaration of Competing Interest

The authors declare the following financial interests/personal relationships which may be considered as potential competing interests:

Vivian Y S Lee reports support provided by TMD Technologies ltd.

Acknowledgements

References

[1] T.G. Karayiannis, M.M. Mahmoud, Flow boiling in microchannels: fundamentals and applications, Appl. Therm. Eng. 115 (2017) 1372–1397.

[2] M.M. Mahmoud, T.G. Karayiannis, Flow boiling in mini to microdiameter channels, in: J.R. Thome (Ed.), Encyclopedia of Two-Phase Heat Transfer and Flow IV, World Scientific Publishing, 2018, pp. 233–301.

[3] S.A. Khan, M.A. Atieh, M. Koç, Micro-nano scale surface coating for nucleate boiling heat transfer: a critical review, Energies 11 (11) (2018) 1–30.

[4] M. Shojaeian, A. Koşar, Pool boiling and flow boiling on micro- and nanostructured surfaces, in: Experimental Thermal and Fluid Science, 63, Elsevier Inc., 2015, pp. 45–73.

[5] G. Liang, I. Mudawar, Review of channel flow boiling enhancement by surface modification, and instability suppression schemes, Int. J. Heat Mass Transf. 146 (2020) 118864.

[6] J.M. Kim, T.J. Kim, D.I. Yu, H. Noh, M.H. Kim, K. Moriyama, H.S. Park, Effect of heterogeneous wetting surface characteristics on flow boiling performance, Int. J. Heat Fluid Flow 70 (2018) 141–151.

[7] V. Khanikar, I. Mudawar, T.S. Fisher, Flow boiling in a micro-channel coated with carbon nanotubes, IEEE Trans. Components Packag. Technol. 32 (3) (2009) 639–649.

[8] C.S. Sujith Kumar, S. Suresh, L. Yang, Q. Yang, S. Aravind, Flow boiling heat transfer enhancement using carbon nanotube coatings, Appl. Therm. Eng. 65 (1–2) (2014) 166–175.

[9] A.K.M.M. Morshed, T.C. Paul, J.A. Khan, Effect of Al2O3 nanoparticle deposition on flow boiling performance of water in a microchannel, Exp. Therm. Fluid Sci. 47 (2013) 6–13.

[10] Y.J. Choi, D.H. Kam, Y.H. Jeong, Analysis of CHF enhancement by magnetite nanoparticle deposition in the subcooled flow boiling region, Int. J. Heat Mass Transf. 109 (2017) 1191–1199.

[11] A. Kosar, K. Chih, J. Kuo, and Y. Peles, "Suppression of Boiling Flow Oscillations in Parallel Microchannels by Inlet Restrictors," 2006.

[12] S.K. Oudah, R. Fang, A. Tikadar, A.S. Salman, J.A. Khan, An experimental investigation of the effect of multiple inlet restrictors on the heat transfer and pressure drop in a flow boiling microchannel heat sink, Int. J. Heat Mass Transf. 153 (2020) 119582.

[13] Y.Y. Hsu, On the size range of active nucleation cavities on a heating surface, J. Heat Transfer 84 (3) (1962) 207–213.

[14] D. Deng, L. Chen, W. Wan, T. Fu, X. Huang, Flow boiling performance in pin fin- interconnected reentrant microchannels heat sink in different operational conditions, Appl. Therm. Eng. 150 (2019) 1260–1272.

[15] J. Zeng, S. Zhang, Y. Tang, Y. Sun, W. Yuan, Flow boiling characteristics of micro-grooved channels with reentrant cavity array at different operational conditions, Int. J. Heat Mass Transf. 114 (2017) 1001–1012.

[16] Y. Sun, L. Zhang, H. Xu, X. Zhong, Subcooled flow boiling heat transfer from microporous surfaces in a small channel, Int. J. Therm. Sci. 50 (6) (2011) 881–889.

[17] Y. Sun, L. Zhang, H. Xu, X. Zhong, Flow boiling enhancement of FC-72 from microporous surfaces in minichannels, Exp. Therm. Fluid Sci. 35 (7) (2011) 1418–1426.

[18] P. Bai, T. Tang, B. Tang, Enhanced flow boiling in parallel microchannels with metallic porous coating, Appl. Therm. Eng. 58 (1–2) (2013) 291–297.

[19] Y.K. Prajapati, P. Bhandari, Flow boiling instabilities in microchannels and their promising solutions – A review, Exp. Therm. Fluid Sci. 88 (2017) 576–593.

[20] F. Yang, X. Dai, Y. Peles, P. Cheng, C. Li, Can multiple flow boiling regimes be reduced into a single one in microchannels? Appl. Phys. Lett. 103 (043122) (2013).

[21] F. Yang, W. Li, X. Dai, C. Li, Flow boiling heat transfer of HFE-7000 in nanowire-coated microchannels, Appl. Therm. Eng. 93 (2016) 260–268.

[22] S. Wang, H.H. Chen, C.L. Chen, Enhanced flow boiling in silicon nanowire–coated manifold microchannels, Appl. Therm. Eng. 148 (2019) 1043–1057.

[23] D. Li, G. S. Wu, W. Wang, Y. D. Wang, D. Liu, D. C. Zhang, Y. F. Chen, G. P. Peterson, and R. Yang, "Enhancing Flow Boiling Heat Transfer in Microchannels for Thermal Management with Monolithically-Integrated Silicon Nanowires," 2012.

[24] S. Bortolin, A. Francescon, G. Ribatski, D. Del Col, Flow boiling of R134a and HFE-7000 in a single silicon microchannel with microstructured sidewalls, Int. J. Heat Mass Transf. 179 (2021) 121653.

[25] V.Y.S. Lee, T.G. Karayiannis, Effect of inlet subcooling on flow boiling in microchannels, Appl. Therm. Eng. 181 (2020) 115966.

[26] F.P. Incropera, T.L. Bergman, D.P. DeWitt, A.S. Lavine, Fundamentals of Heat and Mass Transfer, 7th Edition, John Wiley & Sons, 2012.

[27] R.K. Shah, A.L. London, Laminar Flow Forced Convection in Ducts: A Source Book for Compact Heat Exchanger Analytical Data, 1st ed., Academic Press, 1978.

[28] W. Hugh, W. Coleman, Experimentation, Validation, and Uncertainty Analysis for Engineers, 3rd Edition, John Wiley & Sons, Glenn, Steele, 2009.

[29] V. Y. S. Lee, "Flow Boiling of HFE-7200 in Multi-Microchannel Heat Sinks for High-Heat Flux Applications," PhD thesis, Brunel University London, 2020.

[30] X.F. Peng, G.P. Peterson, Convective heat transfer and flow friction for water flow in microchannel structures, Int. J. Heat Mass Transf. 39 (12) (1996) 2599–2608.

[31] K. Stephan, P. Preusser, Wärmeübergang Und Maximale Wärmstromichte Beim Behältersieden Binärer Und Ternärer Flüssigkeitsgemische, Chem. Ing. Tech. 51 (37) (1979).

[32] N. Borhani, J.R. Thome, Intermittent dewetting and dryout of annular flows, Int. J. Multiph. Flow 67 (2014) 144–152.

[33] P. Balasubramanian, S.G. Kandlikar, Experimental Study of Flow Patterns, Pressure Drop, and Flow Instabilities in Parallel Rectangular Minichannels, Heat Transf. Eng. 26 (3) (2005) 20–27.

[34] A.H. Al-Zaidi, M.M. Mahmoud, T.G. Karayiannis, Flow boiling of HFE-7100 in microchannels: Experimental study and comparison with correlations, Int. J. Heat Mass Transf. 140 (2019) 100–128.

[35] John G. Collier, John R. Thome, *Convective Boiling and Condensation*, Third, Clarendon Press, 1996.

[36] M.M. Mahmoud, T.G. Karayiannis, Flow pattern transition models and correlations for flow boiling in mini-tubes, Exp. Therm. Fluid Sci. 70 (2016) 270–282.

[37] J.R. Thome, V. Dupont, A.M. Jacobi, Heat transfer model for evaporation in microchannels. Part I: Presentation of the model, Int. J. Heat Mass Transf. (2004).

[38] J.R. Thome, L. Consolini, Mechanisms of boiling in micro-channels: Critical assessment, Heat Transf. Eng. 31 (4) (2010) 288–297.

[39] D. Euh, B. Ozar, T. Hibiki, M. Ishii, C.-H. Song, Characteristics of Bubble Departure Frequency in a Low-Pressure Subcooled Boiling Flow, J. Nucl. Sci. Technol. 47 (7) (2010) 608–617.

[40] I. Mudawar, Two-phase microchannel heat sinks: Theory, applications, and limitations, J. Electron. Packag. Trans. ASME 133 (4) (2011).

[41] Y. Liu, D.F. Fletcher, B.S. Haynes, On the importance of upstream compressibility in microchannel boiling heat transfer, Int. J. Heat Mass Transf. 58 (1–2) (2013) 503–512.

[42] S. Gedupudi, D.B.R. Kenning, T.G. Karayiannis, Flow Boiling in Rectangular Microchannels: 1-D Modeling of the Influence of Inlet Resistance on Flow Reversal, Heat Transf. Eng. 37 (13–14) (2016) 1114–1125.